EEG state-trajectory instability and speed reveal global principles of intrinsic spatiotemporal neural dynamics

Melisa Menceloglu, Marcia Grabowecky, & Satoru Suzuki
Northwestern university, Evanston, IL, U.S.A.

Send correspondences to:
Satoru Suzuki
Northwestern University
Department of Psychology
Interdepartmental Neuroscience
2029 Sheridan Road, Evanston, IL 60208
Phone: (847)467-1271
Email: satoru@northwestern.edu

Abstract

The spatiotemporal dynamics of EEG/MEG (electro/magnitoencephalogram) have typically been investigated by applying time-frequency decomposition and examining power-power, phase-phase, or power-phase correlations between combinations of frequency bands and scalp sites, primarily to identify neural correlates of behaviors and traits. Instead, we directly extracted global EEG spatiotemporal dynamics as the trajectories of *k*-dimensional (*k* = the number of scalp sites) state vectors to investigate potential global principles governing neural dynamics. We chose time-scale dependent trajectory instability (approximately the 2nd temporal derivative) and speed (approximately the 1st temporal derivative) as state variables, that characterized trajectory shapes. We compared trajectories across posterior, central, and anterior scalp regions as their dynamics may serve distinct functions. We recorded EEG while participants engaged in spontaneous thoughts with their eyes closed to investigate intrinsic neural dynamics. Some potential global principles emerged. The trajectory instability from all three regions tightly converged at the level of generating nearly unconstrained but slightly conservative turns (on average) at the time-scale of ~25 ms, potentially suggesting that spectral-amplitude profiles are globally adjusted to maintain this convergence. Further, within- and cross-frequency phase relations appear to be coordinated so as to reduce average trajectory speed, increase temporal variations in both trajectory speed and instability in a relatively time-scale invariant manner, and to make global trajectories less oscillatory. Future research may investigate the functional relevance of these intrinsic global-dynamics principles by examining how they adjust to various sensory environments and task demands or remain invariant. The current results also provide macroscopic constraints for quantitative modeling of neural dynamics especially as the time-scale based measures are relatable to oscillatory dynamics.

Introduction

EEG/MEG offer non-invasive methods to study large-scale neural dynamics with millisecond temporal precision (see Varela et al., 2001 for a review). For the purpose of investigating neural dynamics, EEG/MEG from each scalp site is typically decomposed into time series of frequency components (e.g., using a Morlet wavelet transform); temporal associations among spectral powers and/or phases within the same frequency bands and/or across different frequency bands are then examined between pairs of sites. Temporal associations have also been examined between the power of a higher-frequency band (typically γ) and the phase of a lower-frequency band (typically δ-α) either within or across sites. These analyses using time-frequency decomposition have elucidated specific power-power, phase-phase, and/or power-phase couplings within and across sites that may contribute to various perceptual, attentional, and cognitive functions (e.g., Fries, 2005; Palva & Palva, 2007; Duzel, Penny, & Burgess, 2010; Engel & Fries, 2010; Dahaene & Changeux, 2011; Donner & Siegel, 2011; Palva & Palva, 2012; Klimesch, 2012; Jensen, Gips, Bergmann, & Bonnefond, 2014; Michalareas, Vezoli, van Pelt, Schoffelen, Kennedy, & Fries, 2016).

The current study was motivated by a complementary goal. Instead of trying to identify various types of oscillatory coupling as neural correlates of mental activities, we investigated general principles that may govern large-scale spatiotemporal dynamics. We focused on "intrinsic" dynamics reflected in EEG signals recorded while participants engaged in spontaneous thoughts with their eyes closed. Many EEG/MEG studies (also fMRI studies based on inter-region temporal correlations of BOLD signals on a much slower time-scale) examined what is called resting-state activity for diagnostic classification (e.g., Adebimpe, Arabi, Bourel-Ponchel, Mahmoudzadeh, & Wallois, 2016; Antonakakis et al., 2016; Gonzalez et al., 2018) as well as for identifying intrinsic spatial networks of phase-phase, power-power, or power-phase couplings within or between specific frequency bands (e.g., Osipoval, Hermes, & Jensen, 2008; Hipp, Hawellek, Corbetta, Siegel, & Engel, 2012; Müller, Perdikis, Oertzen, Sleimen-Malkoun, Jirsa, & Lindenberger, 2016; Olejarczyk, Marzetti, Pizzella, & Zappasodi, 2017; Stankovski, Ticcinelli, McClintock, & Stefanovska, 2017; Scally, Burke, Bunce, & Delvenne, 2018). While these studies have revealed much in terms of spatial distributions and graph theoretic metrics of power/phase relations, their primary goals were to target specific frequency bands to identify neural correlates of individual differences, dysfunctions, or tasks, or to distinguish spatial networks mediated by different frequency bands. The goal of the current study was complementary in that we aimed to elucidate general quantitative principles that may govern large-scale intrinsic neural dynamics by directly examining EEG spatiotemporal dynamics as multidimensional state vectors (without applying time-frequency decomposition).

We coded EEG from k sites as a k-dimensional state vector $\overrightarrow{V_k}(t)$ (Figure 1A). Global EEG dynamics are entirely captured by the k-dimensional trajectories of a state vector. Large-scale neural processes are likely reflected in how these trajectories evolve. For example, a persistent trajectory movement in the same direction would indicate a continuation of the same process. The degree of directional instability (as a function of time) can be defined for a specific time-scale Δt as the angular change θ in trajectory direction $\frac{\Delta\overrightarrow{V_k}}{\Delta t}$ (the derivative taken over Δt with linear interpolation) across an interval of Δt. This measure is informative because the shape of a state-vector trajectory can be characterized based on how θ depends on Δt. For example, a smoothly curved trajectory is characterized by small θ's for a short Δt and large θ's for a longer Δt (Figure 1B). A rough but overall straight trajectory is characterized by the opposite combination, large θ's for a short Δt and small θ's for a longer Δt (Figure 1C). We thus formally define *trajectory instability* (with a larger value reflecting a greater degree of directional instability of a state trajectory) as,

$$Traj.Ins(t,\Delta t) = \theta\left(\frac{\Delta\overrightarrow{V_k}(t-\Delta t/2)}{\Delta t}, \frac{\Delta\overrightarrow{V_k}(t+\Delta t/2)}{\Delta t}\right) \text{—}Eq.\ 1,$$

where t is time, Δt is time-scale, and θ is the angle between a pair of $\left(\frac{\Delta\overrightarrow{V_k}}{\Delta t}\right)$'s evaluated at $t-\Delta t/2$ and $t+\Delta t/2$, with θ=0° indicating the continuation of a trajectory in the same direction, θ<90° indicating the trajectory largely moving forward, θ=90° indicating an orthogonal turn, and θ>90° indicating the trajectory largely reversing (in k-dimensional space). In addition to the time-scale dependence of trajectory instability, trajectory speed is informative,

$$Traj.Spd(t,\Delta t) = \left|\frac{\Delta\overrightarrow{V_k}(t)}{\Delta t}\right| \text{—}Eq.\ 2,$$

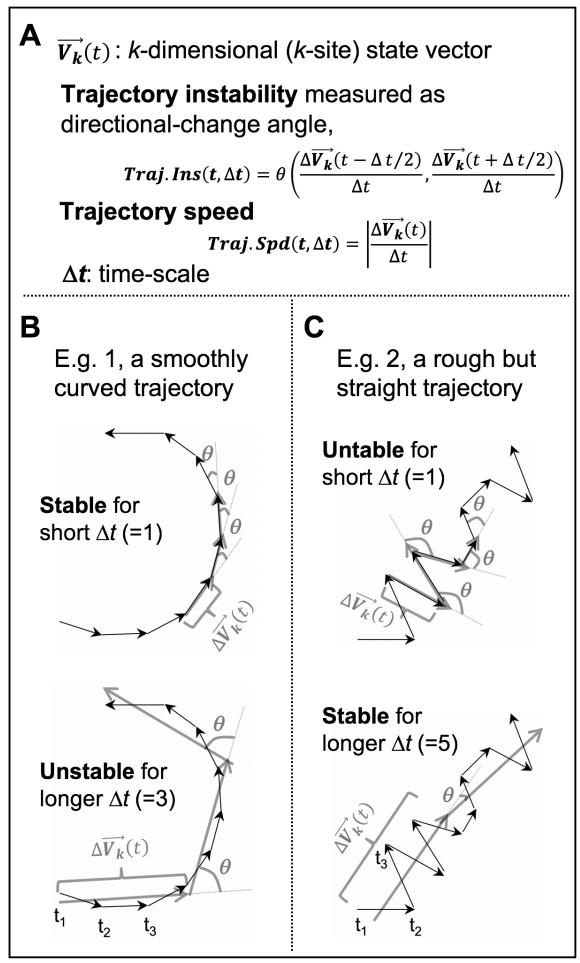

Figure 1. Illustrative examples of k-dimensional (k-site) state trajectories. **A.** Definitions of the relevant variables, state vector, $\overrightarrow{V_k}(t)$, trajectory instability, $Traj.Ins(t,\Delta t)$ trajectory speed, $Traj.Spd(t,\Delta t)$,and time-scale, Δt. **B, C.** Each black arrow illustrates the temporal derivative of a state vector, $\frac{d\overrightarrow{V_k}(t)}{dt}$, measured in the smallest temporal resolution (512 Hz). Each gray arrow represents a state-trajectory differential, $\Delta\overrightarrow{V_k}(t)$, linearly interpolated over Δt, so that dividing it by Δt gives trajectory velocity, $\frac{\Delta\overrightarrow{V_k}(t)}{\Delta t}$, whose magnitude is trajectory speed for time-scale, Δt, at time, t. The angle, θ, between a pair of $\frac{\Delta\overrightarrow{V_k}(t)}{\Delta t}$ evaluated at $t\pm\Delta t/2$ represents trajectory instability for time-scale, Δt, at time, t. **B.** A smoothly curved trajectory is characterized by small θ values for a short Δt (=1) and large θ values for a longer Δt (=3). **C.** A rough but straight trajectory is characterized by large θ values for a short Δt (=1) and small θ values for a longer Δt (=5).

where a larger value indicates a greater rate at which the trajectory moves in the direction of $\frac{\Delta \overrightarrow{V_k}(t)}{\Delta t}$ in the time-scale of Δt.

We divided the 64 scalp sites into posterior, central, and anterior regions because these regions may reflect relatively distinct processes that may require different dynamics. The posterior region may primarily reflect visual processes (including attention and working memory), the central region may primarily reflect auditory, linguistic, mnemonic, and motor processes (also including attention and working memory), and the anterior region may reflect cognitive, regulatory, attentional, and decisional processes (e.g., Laufs et al., 2003; Jann et al., 2010; Luck & Kappenman, 2012; Pratt, 2011; Smulders, Miller, & Luck, 2012; Swaab, Ledoux, Camblin, & Boudewyn, 2012).

We applied the trajectory-instability and trajectory-speed analyses to the resting-state EEG data to elucidate potential general principles governing large-scale intrinsic neural dynamics.

Methods

Participants. Twenty-four Northwestern University students (15 female, 8 male, and 1 non-binary; ages 18 to 24 years, *M*=21.25, *SD*=1.57) gave informed consent to participate for monetary compensation ($10/hr). All were right-handed, had normal hearing and normal or corrected-to-normal vision, and had no history of concussion. They were tested individually in a dimly lit room. The study protocol was approved by the Northwestern University Institutional Review Board.

EEG recording procedures and preprocessing. EEG signals were recorded from 64 scalp electrodes at a sampling rate of 512 Hz using a BioSemi ActiveTwo system (see www.biosemi.com for details) for about 5 minutes while participants engaged in spontaneous thoughts with their eyes closed. Two additional electrodes were placed on the left and right mastoid area. The EEG data were preprocessed with MATLAB using the EEGLAB and ERPLAB toolboxes (Delorme & Makeig, 2004; Lopez-Calderon & Luck, 2014). Data were re-referenced offline to the average of the two mastoid electrodes, bandpass-filtered at 0.01-80 Hz, and notch-filtered at 60 Hz (to remove power-line noise that affected the EEG data from some of the participants). To reduce the effects of volume conduction and reference electrode choices, as well as to facilitate data-driven EEG source discrimination, we applied the surface-Laplacian transform to all EEG data (Hjorth, 1980; Kayser and Tenke, 2006; Tenke and Kayser, 2012) using Perrin et al.'s method (e.g., Perrin, Pernier, Bertrand, Giard, & Echallier, 1987; Perrin, Pernier, Bertrand, & Echallier, 1989a; 1989b) with a typical set of parameter values (Cohen, 2014). Here we refer to surface-Laplacian transformed EEG simply as EEG.

EEG data analysis. The continuous EEG data were segmented into 58-59 (depending on the participants) 5-s intervals for several reasons. As we focused on neural dynamics in the sub-second time-scale, the segmenting allowed us to generate phase-scrambled control data every 5 seconds so that the control data closely tracked any gradual (~0.5 Hz or slower) changes in spectral-amplitude profiles. As behavioral tasks often use experimental trials lasting several seconds, intrinsic neural dynamics analyzed in 5-s intervals would be conducive to comparisons with results obtained in typical cognitive neuroscience experiments. The segment-wise analysis also allowed us to evaluate the stability of intrinsic global dynamics over the 5-min period.

While phase-scrambling can be performed using several different methods, we chose discrete cosine transform, DCT (e.g., Kiya et al., 2010). In short, we transformed each 5-s EEG waveform with type-2 DCT, randomly shuffled the signs of the coefficients, and then inverse-transformed it with type-3 DCT, which yielded a phase-scrambled version. DCT-based phase-scrambling is similar to DFT (discrete Fourier transform) -based phase-scrambling except that it is less susceptible to edge effects especially when phase-scrambling needs to be performed on relatively short waveforms.

We divided the scalp into three regions. The posterior region included *Oz*, *O1*, *O2*, *POZ*, *PO3*, *PO4*, *PO7*, *PO8*, *Pz*, *P1*, *P2*, *P3*, *P4*, *P5*, *P6*, *P7*, and *P8* (the gray region in Figure 2E); the central region included *CPZ*, *CP1*, *CP2*, *CP3*, *CP4*, *Cz*, *C1*, *C2*, *C3*, *C4*, *C5*, *C6*, *FCZ*, *FC1*, *FC2*, *FC3*, and *FC4* (the blue region in Figure 2E); the anterior region included *Fz*, *F1*, *F2*, *F3*, *F4*, *F5*, *F6*, *F7*, *F8*, *AFZ*, *AF3*, *AF4*, *AF7*, *AF8*, *FpZ*, *Fp1*, and *Fp2* (the red region in Figure 2E). Note that each region contained 17 sites. For measures of state-trajectory instability and speed to be commensurate across the three regions, the number of dimensions (i.e., the number of sites) needed to be matched across the regions.

Time-averaged spectral-amplitude profiles (computed per 5-s segment and averaged across all segments per participant, then averaged across participants) from the three regions are shown in Figure 2. All spectral-amplitude profiles included the typical $1/f^{\beta}$ component that partly reflects an Ornstein-Uhlenbeck process which is a part of the standard integrate-and-fire model of a neuron, accounting for the stochastic membrane-potential dynamics in the absence of input currents (e.g., Koch, 1999; Mazzoni et al., 2008; see He, 2014, for a review of the various contributing factors). As expected from EEG recordings with the eyes closed, the posterior spectral-amplitude profiles included pronounced α (~10 Hz) peaks (the black curves in Figure 2) that were reduced in the central profiles (the blue curves in Figure 2) and virtually absent in the anterior profiles (the red curves in Figure 2).

The global spatiotemporal dynamics of each region was represented by the corresponding 17-dimensional state vector $\overrightarrow{V_k}(t)$ sampled at 512 Hz. State-trajectory instability and speed were evaluated as a function of time

t and time-scale Δt by first computing the temporal derivative $\frac{\Delta\overrightarrow{V_k}(t)}{\Delta t}$ (the linear fit to $\overrightarrow{V_k}(t)$ computed over $t\pm\Delta t/2$) as a function of t for a range of Δt values. The smallest Δt was two time-points (where each time-point was 1/512 s at the sampling rate of 512 Hz) or ~3.9 ms, with subsequent Δt values increased by integer multiples of ~3.9 ms, with the largest Δt being 60 times as long as the smallest Δt, or ~234 ms. State-trajectory instability at time t for a time-scale Δt was then evaluated as the angle θ between $\frac{\Delta\overrightarrow{V_k}(t-\Delta t/2)}{\Delta t}$ and $\frac{\Delta\overrightarrow{V_k}(t+\Delta t/2)}{\Delta t}$, which was computed as,

$$Traj.Ins(t,\Delta t) = acos\left[\frac{\left(\frac{\Delta\overrightarrow{V_k}(t-\Delta t/2)}{\Delta t}\right)\cdot\left(\frac{\Delta\overrightarrow{V_k}(t+\Delta t/2)}{\Delta t}\right)}{\left|\frac{\Delta\overrightarrow{V_k}(t-\Delta t/2)}{\Delta t}\right|\left|\frac{\Delta\overrightarrow{V_k}(t+\Delta t/2)}{\Delta t}\right|}\right] \text{—}Eq.\ 3$$

State-trajectory speed at time t for a time-scale Δt was evaluated as,

$$Traj.Spd(t,\Delta t) = \left|\frac{\Delta\overrightarrow{V_k}(t)}{\Delta t}\right| \text{—}Eq.\ 4.$$

Theoretically, both trajectory instability and speed may depend on phase-independent spectral-amplitude profiles (e.g., reduced high-frequency amplitudes would generate smoother trajectories regardless of phase relations) as well as phase relations. Comparisons with phase-scrambled controls (see above) allowed us to isolate the phase-dependent aspects of state-trajectory instability and speed indicative of active phase coordination.

Depending on the analysis, we computed the temporal average and standard deviation of trajectory instability and speed or the temporal correlation between trajectory instability and speed (for both real data and phase-scrambled controls), each as a function of Δt. These statistics were first computed for each 5-s interval and then averaged across all (or subsets of) intervals per participant. All statistical analyses were conducted using participant as the random effect.

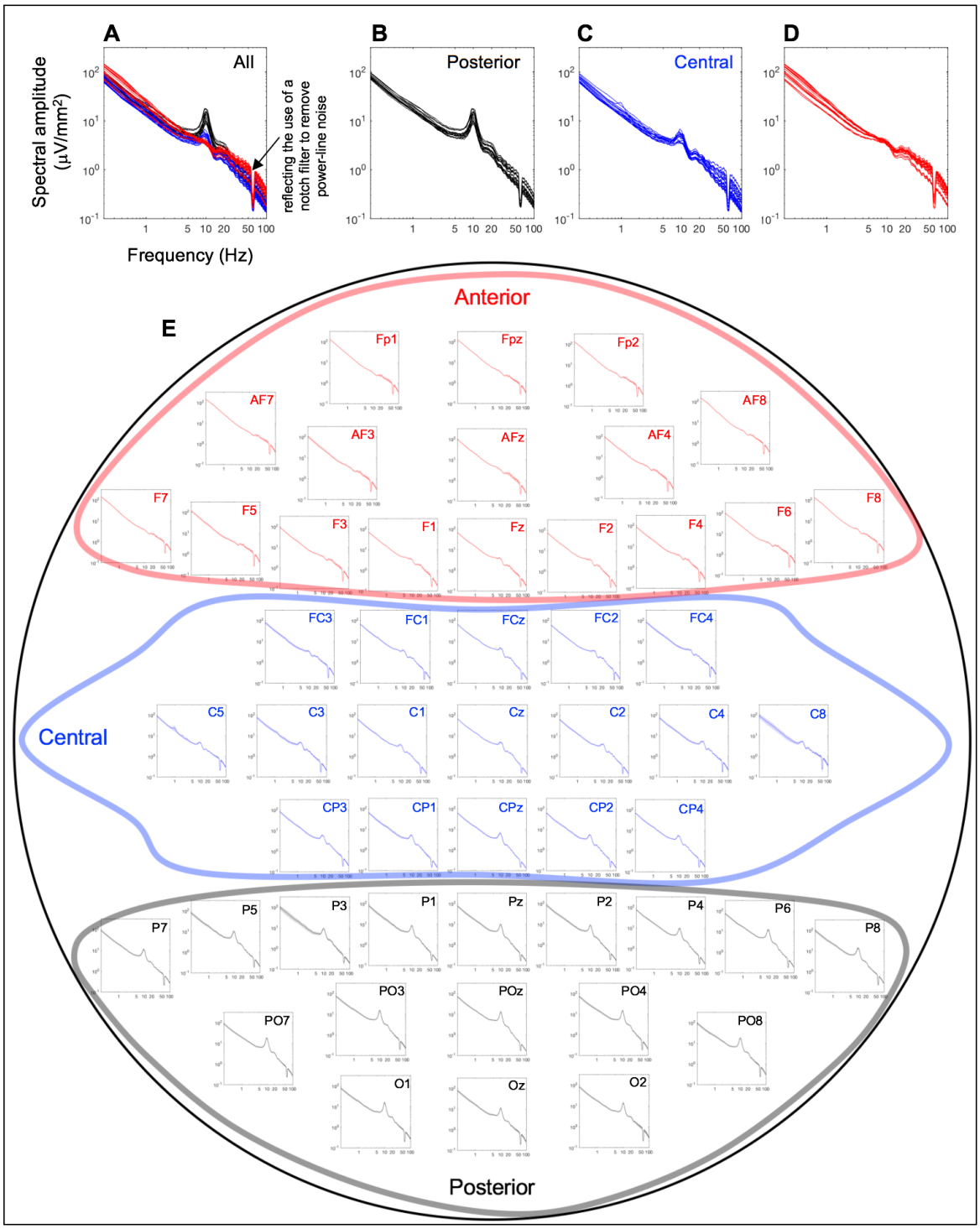

Figure 2. Time-averaged spectral-amplitude profiles for the posterior (black), central (blue), and anterior (red) scalp regions, with each curve representing data from a single site. The dips at 60 Hz reflect the use of a notch filter to remove power-line noise. **A.** Time-averaged spectral-amplitude profiles for all three regions. **B-D.** Time-averaged spectral-amplitude profiles for the posterior (**B**), central (**C**), and anterior (**D**) regions. **E.** Time-averaged spectral-amplitude profiles for individual sites presented within an approximate scalp map.

Results

Effects of spectral-amplitude profiles

State-trajectory instability was characteristically different across the posterior, central, and anterior regions (Figure 3A). In the shorter time-scale (Δt<~25 ms), state trajectories were most stable in the posterior region, intermediate in the central region, and least stable in the anterior region, whereas the pattern flipped in the intermediate time-scale (Δt=25-80 ms). Each horizontal line at the bottom of Figure 3A indicates the time-scale ranges in which trajectory instability significantly ($p < 0.05$ with Bonferroni correction) differed between a pair of regions (blue: posterior vs. central; red: posterior vs. anterior; purple: central vs. anterior). Notably, the levels of trajectory instability in all regions converged at the time-scale of Δt~25 ms at an instability level of ~100°. The convergence was tight as indicated by the narrow inter-participant distribution of the critical time-scales Δt (within 22-30 ms; Figure 3B) that minimized the inter-region differences in trajectory instability (measured as standard deviation), by the narrow distribution of trajectory-instability levels (within 97°-110°; Figure 3C) at the critical time-scale, and by the high precision of convergence, typically yielding the inter-region trajectory-instability differences (measured as standard deviation) of only ~1° at the critical time-scale (Figure 3D). This tight inter-region convergence of the level of state-trajectory instability at the time-scale of ~25 ms is primarily a characteristic of baseline spectral-amplitude profiles independent of phase relations (see below).

State-trajectory speed overall diminished with increasing time-scale Δt (Figure 3E). Otherwise, the trajectory speed for the posterior region was faster than that for the central region across all time-scales examined (see the blue horizontal line at the bottom of Figure E indicating the Δt range of statistically significant difference) and also faster than the trajectory speed for the anterior region in the 20-120 ms time-scale (see the red horizontal line at the bottom of Figure 3E). This inter-region profile of state-trajectory speed is also primarily a characteristic of baseline spectral-amplitude profiles independent of phase relations (see below).

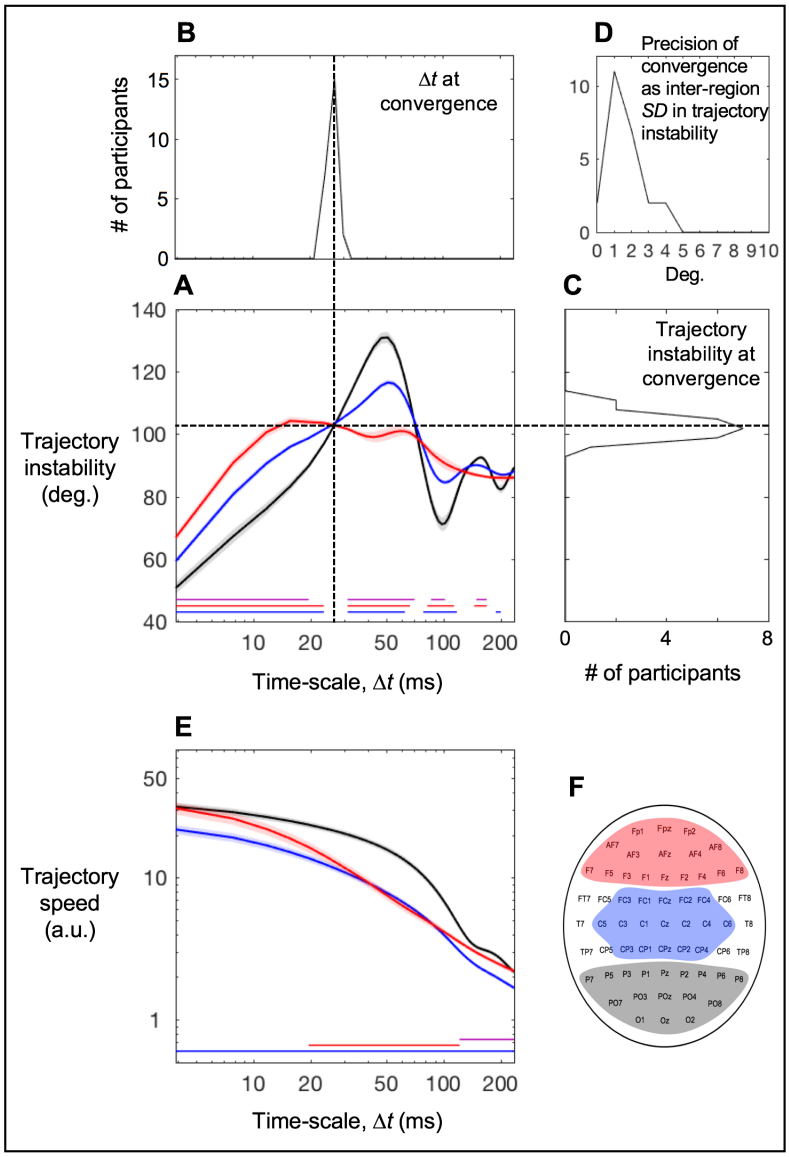

Figure 3. Trajectory instability and speed as a function of time-scale Δt. **A-D.** Trajectory instability. **A.** The main figure showing the time-averaged trajectory instability for the posterior (black), central (blue), and anterior (red) regions (illustrated in **F**) as a function of Δt. Each horizontal line at the bottom indicates the time-scale ranges in which trajectory instability significantly differed between a pair of regions (blue: posterior vs. central, red: posteror vs. anterior, and purple: central vs. anterior) ($p<0.05$ with Bonferroni correction). Notably, the three curves tightly converge at Δt~25 ms where the level of trajectory instability is ~100° (vertical and horizontal dashed lines). To illustrate the consistency of this convergence across participants, the inter-participant distributions (histograms) of Δt values and trajectory-instability levels at the convergence are shown in **B** and **C**, respectively. To illustrate the precision of convergence, the inter-participant distribution of inter-region trajectory-instability differences (as *SD*) at the convergence is shown in **D** (mostly 1° and all less than 5°). **E.** The time-averaged trajectory speed for the posterior (black), central (blue), and anterior (red) regions as a function of Δt. Each horizontal line at the bottom indicates the time-scale ranges in which trajectory speed significantly differed between a pair of regions (blue: posterior vs. central, red: posteror vs. anterior, and purple: central vs. anterior) ($p<0.05$ with Bonferroni correction). The error bars represent ±1 standard error of the mean adjusted for within-participants comparisons (Morey, 2008).

Effects of phase relations

Comparing the real trajectory instability and speed with those computed with the corresponding phase-scrambled controls reveals trajectory characteristics that depend on spectral-phase relations over and above baseline spectral amplitudes. The phase-dependent variations in time-averaged trajectory instability were small for all regions, limited to less than ±2° (Figure 4A), indicating that the characteristic regional profiles of time-averaged trajectory instability including the tight convergence at Δt~25 ms (Figure 3A) primarily reflect baseline spectral-amplitude profiles. Nevertheless, phase relations produced some consistent effects on trajectory instability. The posterior region yielded significantly increased instability (relative to the phase-scrambled control) in the shorter ~8–12 ms and longer ~110–140 ms time-scales (the black curve in Figure 4A). The central region generated a similar pattern but the deviation from the phase-scrambled control was statistically significant only at ~15 ms time-scale (the blue curve in Figure 4A). The anterior region yielded significantly reduced instability at the shortest 4 ms time-scale, but the level of trajectory instability was otherwise equivalent to the phase-scrambled control providing no evidence of active coordination of phase relations. In Figure 4, the lines (dashes or dots) at the top of each panel indicate the time-scale ranges in which the relevant values for specific regions (color-coded in Figure 4F) significantly deviated from the corresponding phase-scrambled controls; the lines (dashes or dots) at the bottom indicate the time-scale ranges in which the values were significantly different between pairs of regions (blue: posterior vs. central; red: posterior vs. anterior; purple: central vs. anterior) (p<0.05 with Bonferroni correction).

While phase relations had overall small effects on time-averaged trajectory instability (Figure 4A), they substantially reduced time-averaged trajectory speed in all regions. Further, the amounts of the speed reduction were similar across time-scales in dB for all regions (Figure 4C). This suggests that similar mechanisms of phase coordination divisively reduce trajectory speed in all regions.

Active control of phase relations, which includes synchronization and desynchronization, likely increases temporal variations in trajectory instability and speed (see the Discussion section for details). Accordingly, the temporal variations (measured as temporal standard deviations) in both trajectory instability (Figure 4B) and speed (Figure 4D) were substantially elevated in all regions (relative to the phase-scrambled controls). In all regions, the amounts of elevation (in degrees for the instability variation and in dB for the speed variation) were similar across time-scales. In addition, the trajectory-instability variation was most elevated in the posterior region, intermediate in the anterior region, and least elevated in the central region (Figure 4B), while the trajectory-speed variation was similarly elevated in the posterior and anterior regions and less elevated in the central region (Figure 4D).

Given this evidence of coordination of trajectory instability and speed through modulation of phase relations, trajectory instability and speed may be jointly coordinated. Specifically, a positive temporal correlation between trajectory instability and speed would indicate faster trajectories being less stable (and slower trajectories being more stable), a negative correlation would indicate faster trajectories being more stable (and slower trajectories being less stable), and no correlation would suggest independent control of trajectory instability and speed. We obtained the temporal correlations between trajectory instability and speed that reflect active spectral-phase coordination as the Fisher-*Z* transformed Spearman's *r* values (robust against outliers) computed for the real data minus those computed for the phase-scrambled controls. In the posterior, and also to a lesser extent in the central regions, the trajectory instability and speed were positively correlated in the ~15-100 ms time-scale (the black and blue curves in Figure 4E) suggesting that the dynamics in the posterior and central regions are coordinated such that faster trajectories are less stable (and slower trajectories are more stable) in the ~15-100 ms time-scale. In the anterior region, the trajectory instability and speed appear to be independently controlled in the same time-scale range (the red curve in Figure 4E), but they were positively correlated in the fast (Δt < ~8 ms) and slow (Δt > ~200 ms) time-scales.

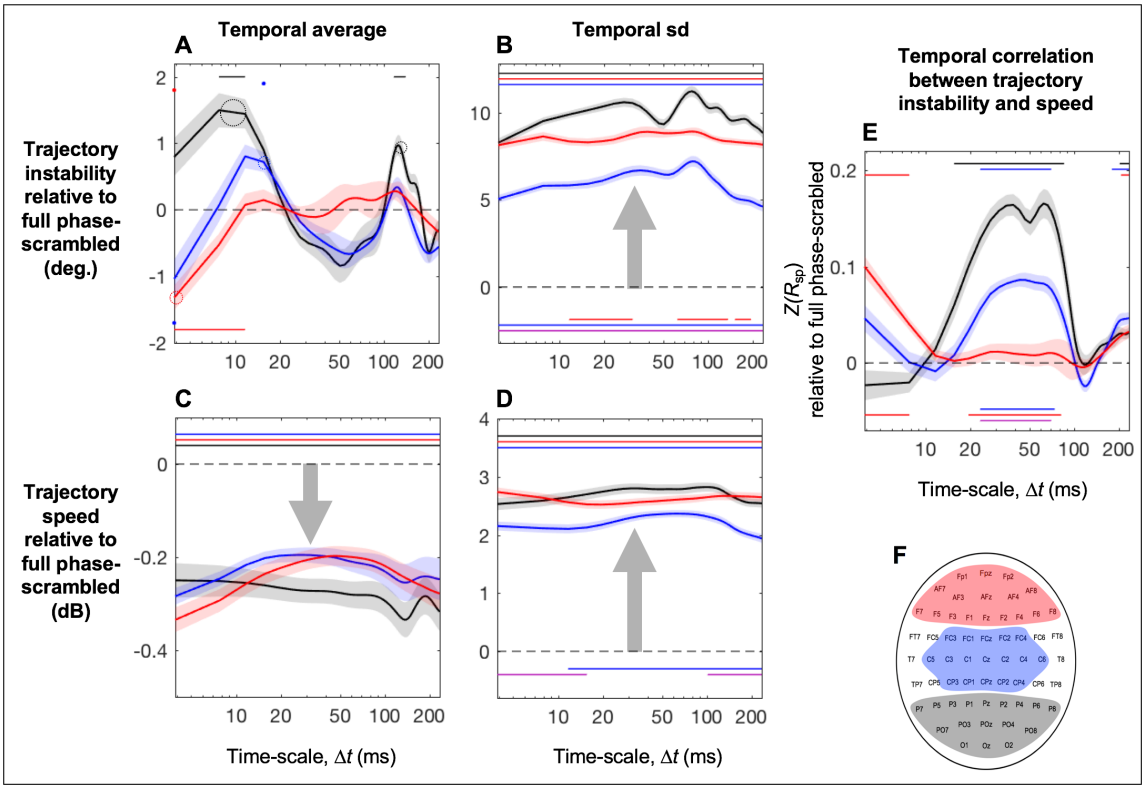

Figure 4. A-D. The phase-relation dependent aspects of trajectory instability and speed as a function of time-scale Δt relative to the corresponding full phase-scrambled controls. **A.** Time-averaged trajectory instability as a function of Δt (real data minus the corresponding phase-scrambled data). **B.** The temporal-variation (measured as standard deviation) in trajectory instability as a function of Δt (real data minus the corresponding phase-scrambled data). **C.** Time-averaged trajectory speed as a function of Δt (real data vs. the corresponding phase-scrambled data in dB). **D.** The temporal variation (measured as standard deviation) in trajectory speed as a function of Δt (real data vs. the corresponding phase-scrambled data in dB). **E.** The temporal correlation between trajectory instability and speed as a function of Δt (real data minus the corresponding phase-scrambled data). In all panels, the data for the posterior, central, and anterior regions are shown in black, blue, and red curves, respectively (illustrated in **F**). Each line (dash or dot) at the top indicates the time-scale ranges in which the correspondingly colored curve significantly differed from the full phase-scrambled control; each line (dash or dot) at the bottom indicates the time-scale ranges in which a pair of curves significantly differed from each other (blue: posterior vs. central, red: posterior vs. anterior, and purple: central vs. anterior) (p<0.05 with Bonferroni correction). The error bars represent ±1 standard error of the mean adjusted for within-participants comparisons (Morey, 2008).

Effects of within-frequency versus cross-frequency phase relations

Phase relations include both within-frequency phase relations—phase relations within the same frequency bands across sites—and cross-frequency phase relations—phase relations between different frequency bands within and across sites. The analyses presented in Figure 4 include the contributions of both types of phase relations because the phase-scrambling procedure randomized spectral phase independently for each frequency component for each site. We examined the unique contributions of cross-frequency phase relations using "cross-frequency phase-scrambled" controls, computed by randomizing phase independently for each frequency component but applying the same set of cross-frequency phase shifts to all sites. This procedure randomized cross-frequency phase relations within and across sites (e.g., X-Hz and Y-Hz components were phase-shifted by Δx and Δy degrees), but preserved within-frequency phase relations across sites (e.g., X-Hz components in all sites were phase-shifted by Δx and Y-Hz components in all sites were phase-shifted by Δy).

The effects of cross-frequency phase relations alone (measured relative to the cross-frequency phase-scrambled controls) were generally smaller than the combined effects of cross- and within-frequency phase relations (measured relative to the full phase-scrambled controls) (Figure 5 vs. Figure 4). Nevertheless, some results are informative. Note that comparisons with the full phase-scrambled controls reflect combined influences of both within- and cross-frequency phase relations, whereas comparisons with the cross-frequency phase-scrambled controls reflect influences of only cross-frequency phase relations. Thus, a unique contribution of within-frequency phase relations may be inferred based on a reliable difference from the full phase-scrambled control with no reliable difference from the cross-frequency phase-scrambled control. A unique contribution of cross-frequency phase relations may be inferred based on reliable but equivalent differences from both the full and cross-frequency phase-scrambled controls. Joint contributions of within- and cross-frequency phase relations may be inferred based on a large reliable difference from the full phase-scrambled control and a smaller but still reliable difference from the cross-frequency phase-scrambled control. We use this logic to interpret the results relative to the full and cross-frequency phase-scrambled controls.

Within-frequency phase relations uniquely contributed to increasing time-averaged trajectory instability in the posterior region in the fast (8–12 ms) time-scale as the increase was reliable relative to the full phase-scrambled control (the black curve at 8-12 ms in Figure 4A) but non-significant relative to the cross-frequency phase-scrambled control (the black curve at 8-12 ms in Figure 5A). However, in the slower time-scale (~120 ms) both within- and cross-frequency phase relations (or cross-frequency phase coordination predominantly) contributed as the somewhat smaller increase in trajectory instability relative to the cross-frequency phase-scrambled control was still reliable (the black curve at ~120 ms in Figures 5A). Cross-frequency phase relations

uniquely contributed to reducing trajectory instability in the anterior region at the fast (~4 ms) time-scale as the reductions were equivalent relative to both the full and cross-frequency phase-scrambled controls (compare the red curves at ~4 ms in Figures 4A and 5A). Both within- and cross-frequency phase relations contributed to the relatively time-scale invariant reductions in time-averaged trajectory speed as the smaller reductions relative to the cross-frequency phase-scrambled control were still reliable (Figures 5C).

Interestingly, within-frequency phase relations uniquely contributed to the substantial and relatively time-scale invariant increases in the temporal variation in trajectory instability as the increases were substantial relative to the full phase-scrambled control (Figure 4B) but were virtually zero relative to the cross-frequency phase-scrambled control (Figures 5B); if anything, cross-frequency phase relations contributed to reducing the temporal variation in trajectory instability in the posterior region in the ~30–50 ms and ~60–75 ms time-scale ranges (the black curve in Figure 5B). Both within- and cross-frequency phase relations contributed to the substantial and relatively time-scale invariant increases in the temporal variation in trajectory speed as the smaller increases relative to the cross-frequency phase-scrambled control was still reliable (Figure 5D).

Both within- and cross-frequency phase relations contributed to the positive temporal correlation between trajectory instability and speed in the ~15-100 ms time-scales in the posterior region as the weaker correlation relative to the cross-frequency phase-scrambled control was still reliable (compare the black curves in Figures 4E and 5E for the ~15-100 ms range). In the Δt<10 ms time-scales, cross- and within-frequency phase relations may have made opposing contributions as the correlation was reliably positive relative to the cross-frequency phase-scrambled control (the black curve at Δt<10 ms in Figure 5E), but it was equivalent to the level of the full phase-scrambled control (the black curve at Δt<10 ms in Figure 4E). This may suggest that in the fast time-scales in the posterior region cross-frequency phase relations promote a positive relationship between trajectory instability and speed while within-frequency phase relations promote a negative relationship between them. Cross-frequency phase relations uniquely contributed to the positive correlation in the central region as the correlations were equivalent relative to both the full and cross-frequency phase-scrambled controls (compare the blue curves in Figures 4E and 5E). Cross-frequency phase relations also uniquely contributed to the positive correlation at the fast (~4 ms) time-scale in the anterior region as the correlations were equivalent relative to both the full and cross-frequency phase-scrambled controls (compare the red curves at ~4 ms in Figures 4E and 5E). It is noteworthy that independent mechanisms of phase coordination appear to influence the temporal variations in trajectory instability and speed in the anterior region for time-scales beyond ~10 ms as the correlations were overall equivalent to both the full and cross-frequency phase-scrambled controls beyond Δt>~10 ms (the red curves in Figures 4E and 5E).

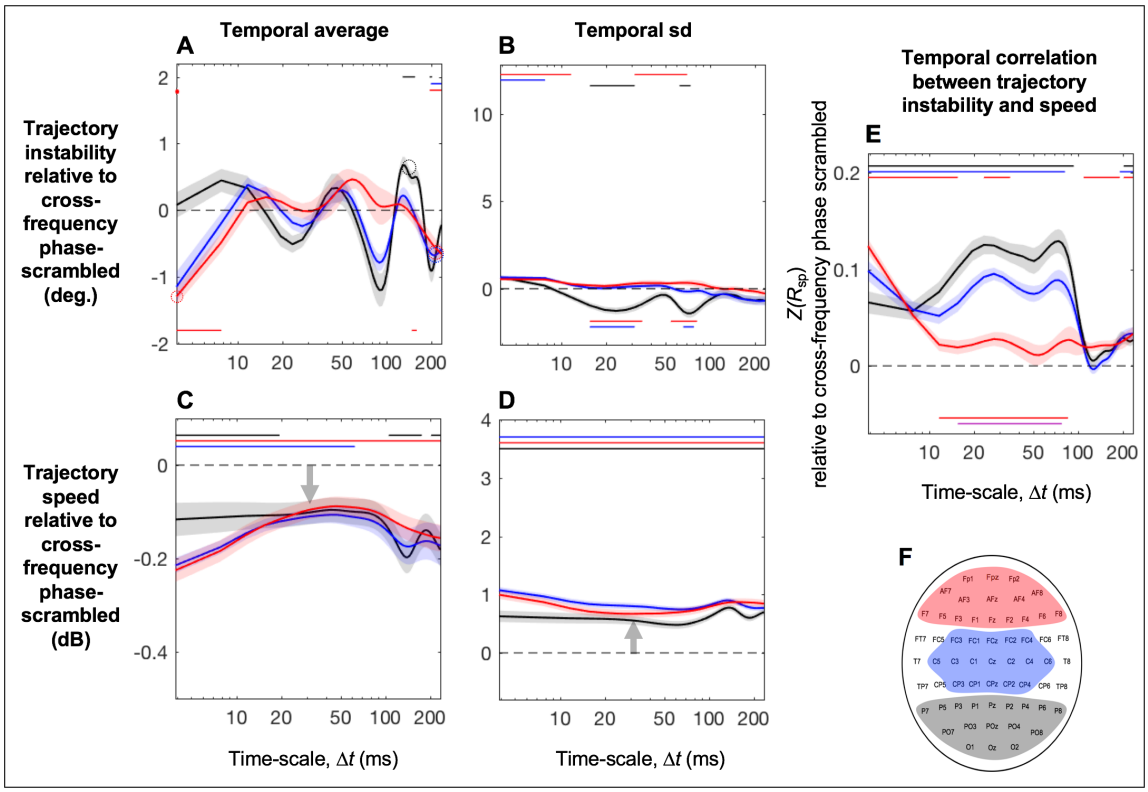

Figure 5. A-D. The cross-frequency-phase-relation dependent aspects of trajectory instability and speed as a function of time-scale Δt, relative to the corresponding cross-frequency phase-scrambled controls (that preserved within-frequency phase relations across scalp sites). **A.** Time-averaged trajectory instability as a function of Δt (real data minus the corresponding phase-scrambled data). **B.** The temporal variation (measured as standard deviation) in trajectory instability as a function of Δt (real data minus the corresponding phase-scrambled data). **C.** Time-averaged trajectory speed as a function of Δt (real data vs. the corresponding phase-scrambled data in dB). **D.** The temporal variation (measured as standard deviation) of trajectory instability as a function of Δt (real data vs. the corresponding phase-scrambled data in dB). **E.** The temporal correlation between trajectory instability and speed as a function of Δt (real data minus the corresponding phase-scrambled data). In all panels, the data for the posterior, central, and anterior regions are shown in black, blue, and red curves, respectively (illustrated in **F**). Each horizontal line (dash or dot) at the top indicates the time-scale ranges in which the correspondingly colored curve significantly differed from the cross-frequency phase-scrambled control; each horizontal line (dash or dot) at the bottom indicates the time-scales in which a pair of curves significantly differed from each other (blue: posterior vs. central, red: posterior vs. anterior, and purple: central vs. anterior) ($p<0.05$ with Bonferroni correction). The error bars represent ±1 standard error of the mean adjusted for within-participants comparisons (Morey, 2008).

Finally, we evaluated the temporal consistency of the results shown in Figures 3-5 by computing the corresponding quantities separately in successive 50-s intervals, dividing each ~5-min EEG recording period into 5 successive intervals (5 curves per region); the data from later intervals are indicated with lighter shades. The time-averaged trajectory instability and speed (presented in Figures 3C and 3E) as a function of time-scale Δt, which are primarily shaped by phase-independent spectral-amplitude profiles (Figure 2), are replotted in Figures 6A and 6B. The full-phase-relation dependent aspects (relative to the full phase-scrambled controls) of the time-averaged trajectory instability and speed, their temporal variations, and their temporal correlations (presented in Figures 4A-4E) as a function of Δt, are replotted in Figures 6C-6G. The cross-frequency-phase-relation dependent aspects (relative to the cross-frequency phase-scrambled controls) of these variables (presented in Figures 5A-5E) are replotted in Figures 6H-6L. It is clear from Figure 6 that all results are reasonably consistent over a ~5-min period with no evidence of systematic drifts.

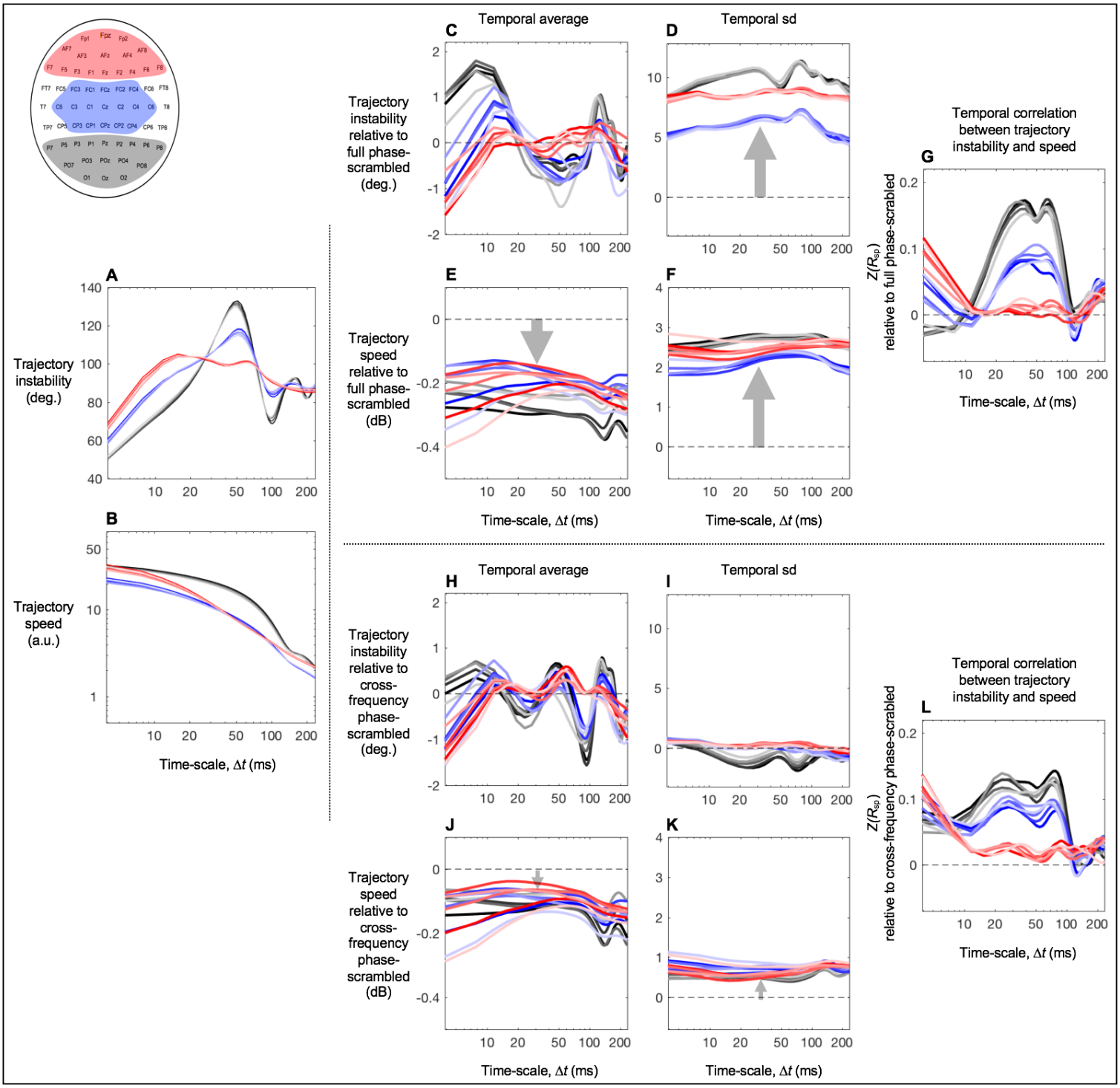

Figure 6. The data shown in Figures 3-5 plotted separately for successive 50-s intervals to show the stability of those data over the ~5-min period. The lighter shades indicate later intervals. **A-B**. The time-averaged trajectory instability and speed as a function of time-scale Δt, corresponding to Figures 3C and 3E. **C-G.** The full-phase-relation dependent aspects of the time-averaged trajectory instability and speed, their temporal variations, and their temporal correlations as a function of time-scale Δt, corresponding to Figures 4A-4E. **H-L.** The cross-frequency-phase-relation dependent aspects of the time-averaged trajectory instability and speed, their temporal variations, and their temporal correlations as a function of time-scale Δt, corresponding to Figures 5A-5E.

Discussion

We investigated the potential principles governing large-scale intrinsic neural dynamics by characterizing the spatiotemporal dynamics of scalp-recorded EEG as the trajectory of a *k*-dimensional state-vector where *k* is the number of scalp sites (with each site containing a current source estimated with the surface-Laplacian transform). We focused on state-trajectory instability and speed as a function of time-scale because these variables succinctly reflect trajectory shapes (Figure 1). Trajectory instability and speed were examined for the posterior, central, and anterior scalp regions because EEG from these regions may reflect distinct processes that may utilize different dynamics (e.g., Laufs et al., 2003; Jann et al., 2010; Luck & Kappenman, 2012; Pratt, 2011; Smulders et al., 2012; Swaab et al., 2012).

Scalp-recorded EEG signals exhibit characteristic spectral-amplitude profiles, generally including a $1/f$-type background profile with embedded peaks at specific frequency bands such as θ, α, and β bands (e.g., see van Albada and Robinson, 2013 for a review; also see Figure 2 for examples from the current study). The $1/f$-type background is thought to reflect random-walk-type neuronal membrane fluctuations (in the absence of input currents) described by an Ornstein-Uhlenbeck process (*Eq*. 5) included in the standard integrate-and-fire model (e.g., Koch, 1999; Mazzoni et al., 2008),

$$\frac{dv(t)}{dt} = -\gamma v(t) + \sqrt{2D} \cdot gn(t) \quad \text{—}Eq.\ 5,$$

where $v(t)$ is the membrane potential, γ is $1/\tau_{\mathrm{m}}$, the reciprocal of the membrane time constant, D is the noise intensity multiplied by γ^2, and $gn(t)$ is Gaussian noise. The membrane potential, $v(t)$, has a monotonically decreasing spectral-power profile, reducing to half power (or $1/\sqrt{2}$ amplitude) at the frequency, $f_{1/2} = \frac{\gamma}{2\pi}$, and approximating a $1/f^2$ power profile (or a $1/f$ amplitude profile) at higher frequencies (see He, 2014, for a review of contributions of this and other mechanisms to the $1/f^{\beta}$ spectral-power profiles). The peaks at specific frequency bands are thought to reflect oscillatory neural activities associated with behavioral operations and/or traits, and much has been revealed about potential roles of oscillatory activities in coordinating neural processes mediating perceptual, attentional, memory, and cognitive operations (e.g., van Beijsterveldt and van Baal, 2002; Fries, 2005; Palva & Palva, 2007; Duzel et al., 2010; Engel & Fries, 2010; Dahaene & Changeux, 2011; Donner & Siegel, 2011; Palva & Palva, 2012; Klimesch, 2012; Jensen et al., 2014; Michalareas et al., 2016; Scally et al., 2018). However, it has been relatively unclear how the diverse spectral-amplitude profiles observed in different brain regions may be spectrally and/or spectrotemporally coordinated in principled ways to maintain

the integrity of global neural dynamics. The current results may contribute to understanding such global principles.

Influences of baseline spectral-amplitude profiles on EEG state-trajectory instability and speed

The time-averaged state-trajectory instability in the posterior, central, and anterior regions tightly converged at the time scale of ~25 ms at the instability level of ~100° (Figures 3A-3D). Because phase relations made minimal contributions to the time-averaged trajectory instability (less than ±2° across all time-scales in all regions; Figure 4A), this convergence reflects inter-region coordination of baseline spectral-amplitude profiles. That is, baseline spectral-amplitude profiles appear to be coordinated across brain regions in such a way that, while state trajectories of different regions make different average degrees of turns on most time-scales, at a universal time-scale of ~25 ms, all state trajectories uniformly make ~100° turns on average, that are near orthogonal (i.e., near 90°) but slightly conservative. This implies that successive topographic changes in the tame-scale of ~25 ms are globally coordinated to be near-maximally unrelated (i.e., near-minimally constrained) but slightly restoring.

How might the time-averaged trajectory instability globally maintained at ~100° at the time-scale of ~25 ms? The time-averaged trajectory-instability as a function of time-scale for each region depends on the exact shapes of the spectral-amplitude profiles at its constituent sites. Nevertheless, there are some factors that make systematic contributions. For example, a Gaussian-random-walk type of EEG activity occurring at all constituent sites would yield a constant level of time-averaged trajectory-instability at 90° regardless of time-scale (making memory free orthogonal turns at all time-scales on average). An oscillatory activity occurring at any of the constituent sites would also make a characteristic contribution. Specifically, an oscillatory component would most strongly contribute to a trajectory's directional changes (which we call instability here) at the time-scale of a half oscillation period because an oscillatory component would make maximal directional changes across half-period intervals. An oscillatory component would minimally contribute to a trajectory's directional changes at the time-scale of a period because an oscillatory component would contribute the same trajectory direction across each period. If EEG at most sites oscillated at the same frequency (i.e., if the overall spatiotemporal pattern of EEG was mostly periodic), the state trajectory would move along an approximate elliptical path[1] so that its average instability would be near 180° at the time-scale of a half period (i.e.,

[1] It would be a planar elliptical path only if EEG at all sites oscillated at the same frequency (with some distribution of phase). Presence of oscillations in other frequencies and the $1/f^{\beta}$ background would distort the elliptical path in a variety of ways. Nevertheless, if oscillations at a specific frequency were dominant across sites relative to other contributions, the path would locally approximate a curved helix.

approximately reversing directions from half period to half period) and near 0° at the time-scale of a period (i.e., approximately moving in the same direction from period to period). Oscillatory directional changes would again optimally impact the state trajectory at the time-scale 1.5 periods, and minimally impact it at the time-scale of 2 periods, and so on, peaking at the odd multiples and dipping at the even multiples of the oscillatory half period. For real EEG data that include a broad range of oscillatory frequencies, the impact of a specific oscillation frequency would diminish for the "higher harmonics" because the directional instability at longer time-scales would be more strongly influenced by slower oscillatory components and slower-varying non-oscillatory components (including the random-walk-type activity that partially underlies the $1/f^{\beta}$ spectral profile).

An example of an oscillatory contribution can be seen in the current results for the posterior region whose constituent sites yielded substantial spectral amplitudes in the α-band (~10 Hz, 50 ms half-period) (the black curves in Figure 2). Based on our reasoning above, the α-band contribution to the time-averaged trajectory instability should peak at the time-scales of 50 ms (a half-period), 150 ms (3 half-periods), etc., and dip at the time-scales of 100 ms (2 half-periods), 200 ms (4 half-periods), etc. This is what we observed (the black curve in Figure 3A). Note that even the largest peak and trough at the half-period and one-period time-scales only reached ~130° and ~75°, respectively (rather than ~180° and ~0°) because of the contributions of other oscillatory frequencies as well as the $1/f^{\beta}$ background (Figure 2), indicating that the overall posterior state trajectory is far from being oscillatory[2]. Similar but less pronounced characteristics were observed in the trajectory instability profile for the central region (the blue curve in Figure 3A), consistent with the fact that the α-band amplitudes were less pronounced at the central sites (the blue curves in Figure 2) relative to the posterior sites. Because oscillations at a specific frequency make their largest contribution to the trajectory instability at the time-scale of a half period, the fact that the central instability was higher than the posterior instability in the short (Δt<~25 ms) time-scales (the blue vs. black curve in Figure 3A) is consistent with the fact that the higher-frequency (>~30 Hz) spectral amplitudes were larger in the central region than in the posterior region (the blue vs. black curves in Figure 2). The fact that the anterior instability was even higher than the

[2] As an alternative way to assess whether the obtained state trajectories were overall oscillatory, we examined the changes in trajectory direction as a function of temporal delay. We chose Δt=~25 ms (not exactly 25 ms due to the 512 Hz sampling rate) for the computation of interpolated trajectory directions (as a function of time) because directional changes in the primary α-band (~10 Hz) oscillatory component would be optimally sensitive to the time-scale of its quarter period (or 25 ms). The average angular difference indeed minimized at the delay of 100 ms (one complete cycle of 10 Hz oscillation) consistent with the primary contributions of α-band oscillations. However, whereas the minimum angular difference across a one-cycle delay should be 0° if the state trajectory was overall oscillatory, even for the posterior region in which the α-band peak was most prominent (Figure 2), the minimum angular difference was 66.3° (se = 2.8°), indicating that the state trajectories shifted by as much as 66.3° (not far from 90°) on average across each α cycle. This confirms that the obtained state trajectories are far from being oscillatory.

central instability in the short (Δt<~25 ms) time-scales (the red vs. blue curve in Figure 3A) is consistent with the fact that the higher-frequency (>~30 Hz) spectral amplitudes were even larger in the anterior than the central region (the red vs. blue curves in Figure 2). The anterior instability profile was relatively flat in the time-scales beyond ~15 ms, consistent with the absence of any substantial spectral peaks (the red curves in Figure 2). Nevertheless, this relatively flat portion reflects oscillatory activities in a broad range of frequencies rather than a dominance by the random-walk-type spectral background because the plateaued instability level was ~100° instead of ~90°. The instability profiles from all regions gradually converged at the level of ~90° in the longer time-scales (Δt>~150 ms), indicating that state trajectories on average make relatively unconstrained directional changes (in the sense that successive topographic changes are maximally unrelated) in the time-scales beyond ~150 ms.

In general, average trajectory-instability levels less than 90° indicate tendencies to move in a forward direction, potentially reflecting strongly driven (e.g., stimulus driven) processes, with 0° indicating continued movements in the same direction, whereas instability levels greater than 90° indicate conservative tendencies to move in a backward direction, potentially reflecting restorative and/or verifying processes, with 180° indicating movement reversals, while instability levels near 90° indicate processes that are relatively unconstrained. From a theoretical perspective, relatively unconstrained but slightly conservative state trajectories may be suitable for frontal brain activity for facilitating flexible changes in cognitive strategies while maintaining some degree of stability. This is consistent with the observed trajectory-instability level of ~100° for the anterior region over a broad range of time-scales (Figure 3C). In contrast, sensory processes may utilize recurrent interactions within ~250 ms to generate reliable perceptual representations that are consistent across the hierarchical sensory representations (e.g., Lamme, Zipser, & Spekreijse, 2002; Fahrenfort, Scholte, & Lamme, 2007). This may be potentially reflected in the instability profiles in the posterior and central regions (roughly reflecting visual and auditory processes, respectively) that include forward movements (<90°), potentially reflecting stimulus driven processes, and backward turns (>90°), potentially reflecting verifying processes, within the time-scale of ~250 ms (Figure 3C).

Given that trajectory instability profiles are sensitive to oscillation amplitudes as well as $1/f^{\beta}$ profiles at constituent sites, the fact that they tightly converged at the level of ~100° at the time-scale of ~25 ms (Figure 3A) may have functional relevance rather than being epiphenomenal. For example, intrinsic neural dynamics may be globally calibrated in such a way that bottom-up sensory and top-down attentional/cognitive processes could exchange information in ~25 ms packets at a matched level of nearly unconstrained but slightly conservative (~100°) state-trajectory flexibility. This matching may facilitate directionally balanced interactions

such that bottom-up and top-down processes contribute on an equal footing to the construction of behaviorally relevant representations of the environment. Because β-band activity (~20 Hz, ~25 ms half-period) would have the largest impact on state-trajectory instability at the convergent time-scale of ~25 ms, an efficient way to maintain this calibration might be to network-wide tune β-band activity to compensate for cross-network variations in multi-frequency oscillatory activity and non-oscillatory activity. While these inferences are highly speculative, the data provide some, though indirect, support for the interpretation that the inter-region convergence of time-averaged trajectory-instability at ~100° at ~25 ms may be actively maintained. If the convergence were actively maintained, the level of trajectory instability should be particularly stable at the critical time-scale of ~25 ms in all three regions. Indeed, both the inter-participant variability of average trajectory instability (Figure 7B) and the within-participant variability across 50-s time intervals (Figure 7C) were minimized at the time-scale of ~25 ms in all three regions. The overall evidence may thus warrant future investigations into the potential mechanisms and functional relevance of this convergence.

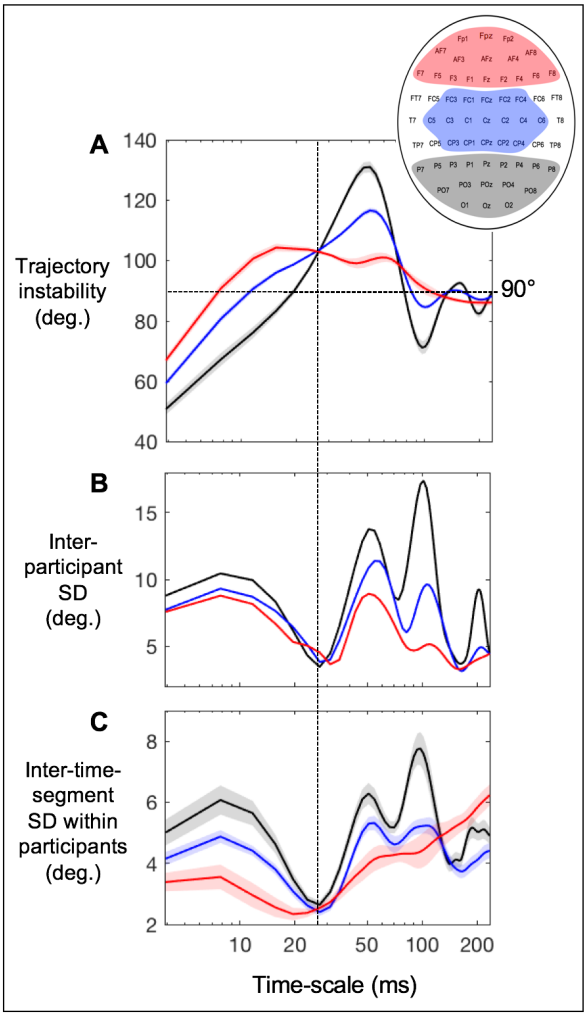

Figure 7. Time-averaged trajectory instability for the posterior (black), central (blue), and anterior (red) regions as a function of time-scale Δt. **A.** Inter-participant averages (the same as Figure 3A). **B.** Inter-participant standard deviations. **C.** Inter-time-interval standard deviations (computed over five 50-s time intervals) averaged across participants. For all three regions, both the between-participant (**B**) and within-participant (i.e., inter-time-interval) (**C**) standard deviations minimized at the time-scale of ~25 ms at which the average trajectory instability from all three regions converged (**A**, vertical dashed line). Note that perturbations in the dimensions orthogonal to the planes of trajectory turns tend to shift the degrees of turns toward 90°; this effect is larger for trajectory turns that are more deviated from 90°. Accordingly, it is observed in **B** and **C** that the standard deviations were particularly elevated at time-scales in which the average trajectory instability substantially deviated from 90° (**A**, horizontal dashed line). The error bars represent ±1 standard error of the mean adjusted for within-participants comparisons (Morey, 2008).

In contrast to the feature-rich profiles of time-averaged trajectory instability, time-averaged trajectory speed largely yielded monotonically decreasing profiles as a function of time-scale for all regions (Figure 3E). Gaussian-random-walk type EEG activity occurring at all sites would yield a power-function profile of time-averaged trajectory speed as a function of time-scale, which would be a negatively sloped line in the log-log

plot, with the intercept proportional to the temporal standard deviation of EEG. An oscillatory activity would contribute maximal directional changes twice per oscillation period. Thus, for time-scales sufficiently shorter than a half-period, the linear-interpolated path segments would relatively closely track the periodic directional changes. However, for time-scales surpassing a half-period, the linear-interpolated path segments would substantially smooth over the periodic directional changes, yielding shorter interpolated trajectories with slower speeds. Thus, an oscillatory component would contribute a relatively constant average speed up to the time-scale of about a half-period, but the contribution would rapidly decrease for longer time-scales. As a result, an oscillatory component would tend to flatten the negatively sloped linear profile of time-averaged trajectory speed (in log-log) for time-scales up to about a half-period, thereby making the profile upwardly bowed with a broad peak trailing the time-scale of a half period. This reasoning is consistent with the fact that the posterior state trajectory with its prominent α-band spectral-amplitude components (the black curves in Figure 2) yielded a substantially bowed trajectory-speed profile with the curvature broadly peaking at the time-scale a little longer than ~50 ms (the black curve in Figure 3E). The degree of bowing is less for the central region (the blue curve in Figure 3E) where the α-band spectral-amplitude components were less prominent (the blue curves in Figure 2). The anterior region with no particularly prominent spectral-amplitude components yielded a relatively linear (in log-log) time-averaged trajectory-speed profile (the red curve in Figure 3E). We note that our use of the notch filter at 60 Hz to remove line noise (see the methods section) caused the general flattening of the time-averaged trajectory-speed profiles (Figure 3E) as well as the general falling of the time-averaged trajectory-instability profiles (Figure 3A) in the faster end of time-scales (Δt<10 ms).

Influences of phase relations

While oscillatory activities increased trajectory instability primarily at half-period time-scales and increased trajectory speed up to about half-period time-scales, their impacts were also modulated by phase relations. We used two types of phase scrambling to infer the contributions of within-frequency and cross-frequency phase relations. Comparisons with the full phase-scrambled controls (EEG from each site independently phase-scrambled) elucidated the joint contributions of within- and cross-frequency phase relations to state-trajectory instability and speed, whereas comparisons with the cross-frequency phase-scrambled controls (EEG from each site phase-scrambled with the same randomization seed) isolated the contributions of cross-frequency phase relations. We inferred a nearly exclusive contribution of within-frequency phase relations when the real data reliably deviated from the full phase-scrambled control but did not reliably deviate from the cross-frequency phase-scrambled control. We inferred a nearly exclusive contribution

of cross-frequency phase relations when the real data reliably and equivalently deviated from both the full and cross-frequency phase-scrambled controls. We inferred contributions of both within- and cross-frequency phase relations when the real data deviated substantially more from the full phase-scrambled control than from the cross-frequency phase-scrambled control but also reliably deviated from the cross-frequency phase-scrambled control.

Broadly speaking, within-frequency phase relations reflect the degree of cross-site phase alignment of oscillatory activity within each frequency band, whereas cross-frequency phase relations reflect within-site EEG waveforms as well as cross-site cross-frequency phase alignments. The fact that our EEG data show similar spectral amplitudes of oscillatory activity across sites within each region (Figure 2) suggests that the obtained trajectory instability and speed profiles were influenced by region-wide phase relations.

Influences of phase relations on EEG state-trajectory instability

We first consider the potential impacts of cross-site within-frequency phase relations on state-trajectory instability, and compare them with the results. At one extreme, if oscillatory activities in a specific frequency band were all phase aligned (i.e., 0° phase lagged) across sites, they would contribute an approximately oscillatory component to a state trajectory. At another extreme, if oscillatory phases were minimally aligned across sites, that is, if phase lags were uniformly distributed between 0° and 180° across sites, the oscillatory activities would contribute an approximately circular[3] component to a state trajectory. An intermediate level of cross-site phase alignment would contribute an approximately elliptical component with a higher (narrower) aspect ratio when the phases are more tightly aligned across sites. Note that phase scrambling would reduce the aspect ratio of these elliptical contributions but would not make them circular because randomized phase distributions would necessarily deviate from uniform distributions[4].

A narrow elliptical component would contribute a large temporal variation in trajectory instability within each oscillatory cycle because directional changes would be large over the two high-curvature portions and small over the two low-curvature portions. Because the high- and low-curvature portions respectively span about a half cycle, an elliptical component would particularly elevate temporal variations in trajectory instability at the quarter-period time-scale (sharply changing directions over the half period containing the high

[3] Strictly speaking, the contribution would be circular only if the oscillation amplitudes were equal across sites. Uneven amplitudes would make the contribution elliptical. Given a specific set of uneven amplitudes, the contribution would have the smallest aspect ratio (i.e., closest to being circular) when the phases of large-amplitude oscillations were evenly distributed between 0° and 180°.
[4] As expected, when artificial data that included oscillatory activities with their phases evenly distributed between 0° and 180° across sites were phase-scrambled, the circular trajectory became elliptical.

curvature and largely moving forward over the half period containing the low curvature). This cyclic variation in trajectory instability would become less pronounced for elliptical components with lower aspect ratios generated by looser cross-site alignments of oscillatory phases because the high and low curvatures would be less different. Thus, tighter cross-site within-frequency phase alignments of oscillatory activities would increase *temporal variations* in trajectory instability especially around the quarter-period time-scale.[5]

In contrast, *time-averaged* trajectory instability is unlikely to be strongly influenced by cross-site within-frequency phase alignments because the average curvature of an elliptical path would be relatively independent of its aspect ratio for a given time-scale.[5] Time-averaged trajectory instability would be influenced by other types of phase relations. For example, an elliptical contribution of a dominant cross-site oscillatory activity in a single frequency band could locally (in time) form a curved helical component in a state trajectory when combined with contributions of oscillatory activities in other frequency bands and the $1/f^{\beta}$ spectral background. In that case, the pitch of the helical trajectory could modulate time-averaged trajectory instability; for example, overall directional changes would be less for a higher-pitched helical trajectory because of the more dominant trajectory movements along the main axis. Nevertheless, detailed considerations of how phase relations within and across frequency bands involving oscillatory and non-oscillatory activities (other than the minimal impact of cross-site within-frequency phase alignments) may influence time-averaged trajectory instability is beyond the scope of this study.

In the current results, the temporal variation in trajectory instability was substantially elevated in a relatively time-scale invariant manner in all regions in such a way that the effect is fully attributable to cross-site within-frequency phase relations (a substantial elevation relative to the full phase-scrambled controls with little deviation from the cross-frequency phase-scrambled controls; Figure 4B vs. Figure 5B). Based on the reasoning above, this elevation in the temporal variation in trajectory instability is consistent with the general tightening of cross-site phase alignments across a broad range of oscillation frequencies. This interpretation is tempered by the fact that volume conduction could have partially mimicked cross-site phase alignments, though we minimized it by applying the surface Laplacian transform (roughly a spatial high-pass filter) to EEG prior to

[5] We have verified that a greater degree of within-frequency phase alignment of cross-site oscillatory activity results in a greater temporal variation in state-trajectory instability (with little effect on its temporal average) especially at the quarter-period time-scale (and its harmonics if no $1/f^{\beta}$ noise is included), using simulated data where EEG at each site was a sine wave oscillating at f Hz while the width of phase distribution was varied. We have also verified that cross-site synchronization of shared random-walk or Gaussian noise results in an increase in the temporal variation in state-trajectory instability with little effect on its temporal average, as well as a reduction in time-averaged trajectory speed in combination with an increase in its temporal variation (relative to the full phase-scrambled controls); these effects are time-scale invariant.

analysis. We later present evidence suggesting that our results indicate real cross-site phase-alignment effects over and above any volume conduction effects (see "Consideration of volume conduction effects").

The above discussion also predicted that time-averaged trajectory instability would be relatively unaffected by tightening of phase alignments, but it might be modulated by contextual effects established by the amplitudes and phases of oscillations in other frequencies and the $1/f^{\beta}$ spectral background. Indeed, the effects of any phase relations (evaluated as deviations from the full or cross-frequency phase-scrambled controls) on the time-averaged trajectory instability were small (less than ±2°). Nevertheless, the results showed some systematic region dependences that may be potentially linked to spectral amplitudes, though we cannot offer any specific hypotheses on mechanisms at this time. For example, major differences in spectral-amplitude profiles among the three regions may be characterized as two broad trends: (1) 10-20 Hz components were most pronounced in the posterior region, intermediate in the central region, and reduced in the anterior region, whereas (2) >30 Hz components were most pronounced in the anterior region, intermediate in the central region, and reduced in the posterior region (Figure 2). Thus, the slight (but reliable) elevation in the time-averaged trajectory instability in the ~10 ms time-scales (observed only against the full phase-scrambled controls) that was most salient in the posterior region (the black curve in Figure 4A), less salient but still observable in the central section (the blue curve in Figure 4A), and absent in the anterior region (the red curve in Figure 4A) may reflect some form of cross-site within-frequency phase coordination of 10-20 Hz components (other than simple phase alignments). Further, the time-averaged trajectory instability in the anterior region that showed little evidence of cross-site within-frequency phase coordination (no more deviated from the full phase-scrambled control than from the cross-frequency phase-scrambled control; the red curves in Figure 4A vs. Figure 5A) may reflect that any cross-site within-frequency phase coordination of >30 Hz components transpire in such a way that it has little effect on time-averaged trajectory instability.

So far, we have considered cross-site *within*-frequency phase coordination, which influenced state trajectories primarily through adjusting cross-site phase alignments within individual frequency bands. Effects of *cross*-frequency phase coordination are more difficult to infer because the cross-frequency phase-scrambling procedure disrupted both within- and cross-site cross-frequency phase relations (while preserving cross-site within-frequency phase relations). Thus, any effects of cross-frequency phase relations measured relative to the cross-frequency phase-scrambled controls may reflect the effects of temporal structures of within-site EEG waveforms (disrupted by the scrambling of within-site cross-frequency relations) and/or the effects of cross-site cross-frequency phase relations (disrupted by the scrambling of cross-site cross-frequency phase relations). Cross-frequency phase relations increased time-averaged trajectory instability at the ~120 ms time-scale in the

posterior region, while it decreased time-averaged trajectory instability at the rapid ~4 ms time-scale in the anterior region (Figure 5A). Further, while the substantial and relatively time-scale invariant increases in the temporal variation in trajectory instability observed across all regions were entirely attributable to within-frequency phase coordination (large elevations relative to the full phase-scrambled controls [Figure 4B] with minimal elevations relative to the cross-frequency phase-scrambled controls [Figure 5B]), cross-frequency phase relations reliably decreased the temporal variation in trajectory instability in the time-scales of 15-30 ms and 60-80 ms in the posterior region (the black curve in Figure 5B). Nevertheless, it is difficult to speculate on how temporal structures of within-site EEG waveform and cross-site cross-frequency phase relations separately or jointly contributed to these effects on state-trajectory instability.

Influences of phase relations on EEG state-trajectory speed

The current results may allow a more coherent understanding of the effects of within- and cross-frequency phase relations on state-trajectory speed. In all three regions, both within- and cross-frequency phase relations (relative to the respective phase-scrambled controls) contributed to decreasing time-averaged trajectory speed (Figures 4C and 4D) while increasing temporal variations in trajectory speed (Figures 5C and 5D). Both the decrease in time-averaged trajectory speed and increase in its temporal variation may be explained by increased cross-site synchronization of EEG (not necessarily oscillatory) waveforms.

Consider a case where each of the k sites made a brief, lasting ΔT, voltage change of Δv within the time period of $N \times \Delta T$. For simplicity, we assume that $N=k$ (i.e., as many brief time periods as the number of sites). At one extreme, if these changes across the k sites occurred completely desynchronously (i.e., each site making the brief change in a separate ΔT interval), the trajectory speed at each ΔT would be constant at $\frac{\Delta v}{\Delta T}$, so that the time-averaged trajectory speed would be, $\frac{\sum_{i=1}^{i=k}\frac{\Delta v}{\Delta T}}{k} = \frac{\Delta v}{\Delta T}$, and the temporal variation in trajectory speed would be zero. At the other extreme, if the changes across the k sites all occurred synchronously within a single ΔT interval, the trajectory speed would be $\frac{\sqrt{\sum_{i=1}^{i=k}\Delta v^2}}{\Delta T} = \frac{\Delta v}{\Delta T} \times \sqrt{k}$ (due to vector summation) within that interval and zero within all other intervals, so that the time-averaged trajectory speed would be $\frac{\frac{\Delta v}{\Delta T}\times\sqrt{k}}{k} = \frac{\Delta v}{\Delta T} \times \frac{1}{\sqrt{k}}$; the temporal variation in trajectory speed (in standard deviation) would be $\frac{\Delta v}{\Delta T} \times \sqrt{k}$. Thus, increased cross-site synchronization of EEG waveforms would both reduce time-averaged trajectory speed (from $\frac{\Delta v}{\Delta T}$ to $\frac{\Delta v}{\Delta T} \times \frac{1}{\sqrt{k}}$ in

this example) and increase its temporal variation (from 0 to $\frac{\Delta v}{\Delta T} \times \sqrt{k}$ in this example).[5] We can also reason that these effects would be enhanced when synchronized EEG changes were sharper (i.e., larger $\frac{\Delta v}{\Delta T}$) and more intermittent (generating a stronger contrast between coincident and silent intervals).

Given these considerations, the large decrease in time-averaged trajectory speed combined with the large increase in its temporal variation relative to the full phase-scrambled controls, that were relatively time-scale invariant in dB (Figures 4C and 4D), are consistent with the interpretation that increased cross-site EEG synchronization (including a broad range of frequency components) contributed to both effects. Although any cross-site synchronization effects could include volume conduction effects (which we minimized by applying the surface Laplacian transform), we later present evidence suggesting that our results indicate real cross-site synchronization effects over and above any volume conduction effects (see "Consideration of volume conduction effects")

We also obtained smaller but reliable decrease in time-averaged trajectory speed combined with its increased temporal variation relative to the cross-frequency phase-scrambled controls (unrelated to any volume conduction effects), that were also relatively time-scale invariant in dB. Based on the preceding discussion, this may suggest that within-site EEG waveforms are coordinated to contain sharper and more intermittent changes at each time-scale (relative to the cross-frequency phase-scrambled controls). This may be analogous to the way in which different spatial-frequency components in natural visual scenes are phase-aligned to generate sharp, high-contrast, and sparse object borders that are relatively scale invariant (i.e., self-similar). Further, the relative time-scale invariance in dB suggests that EEG waveforms are fine-tuned in such a way that time-averaged trajectory speed is divisively reduced while its temporal variation is multiplicatively increased across a broad range of time-scales.

Influences of phase relations on the association between EEG state-trajectory instability and speed

The fact that cross-site coordination of phase relations increased the temporal variations in both trajectory instability and speed is consistent with the fact that phase relations influenced the association between trajectory instability and speed. Overall, we obtained positive temporal correlations between trajectory instability and speed relative to both the full phase-scrambled and cross-frequency phase-scrambled controls. A positive correlation indicates that within- and cross-frequency phase relations are adjusted in such a way that faster trajectories are less directionally stable and slower trajectories are more directionally stable. Further, an oscillatory component would generally contribute a negative correlation (regardless of phase relations) because

the magnitudes of the 1st and 2nd derivatives, reflective of our measures of trajectory speed and instability, are negatively correlated in sinusoidal oscillations. Thus, the generally positive temporal correlations (relative to both types of phase-scrambled controls) suggest that within-frequency and cross-frequency phase relations are adjusted in such a way that global topographic changes are less oscillatory (i.e., more heterogeneous).

In addition to the general positive associations, we obtained some characteristic regional differences. In the posterior and central regions, both within- and cross-frequency phase relations increased the positive correlation in the ~15-100 ms time-scale range (the black and blue curves in Figures 4E and 5E). In the posterior region, within- and cross-frequency phase relations appeared to have had opposing effects in the fast <~10 ms time-scale such that the increased positive correlation driven by cross-frequency phase coordination (the black curve in Figure 5E) was cancelled by the presumably negative correlation driven by within-frequency phase coordination (the black curve in Figure 4E). In the anterior region, cross-frequency phase coordination increased the positive correlation in the fast <~10 ms time-scale (the red curve in Figure 5E). It is noteworthy that there is little evidence of any joint temporal coordination of state-trajectory instability and speed in the anterior region in the ~15-100 ms time-scale range in which the joint coordination was strongest in the posterior and central regions (the red curve vs. black and blue curves in Figures 4E and 5E). Further research is necessary to elucidate the mechanisms underlying these effects.

Consideration of volume conduction effects

The results indicative of cross-site phase alignments in EEG (oscillatory or non-oscillatory) could have been influenced by spurious contributions of volume conduction. The potentially affected results include the elevation of the temporal variation in trajectory instability as well as the reduction of time-averaged trajectory speed and the elevation of its temporal variation. All these effects likely involve the coordination of cross-site within-frequency phase relations such as tightening of phase alignments (see above) that are susceptible to volume conduction effects. We thus re-examined these effects. It has been shown that for a standard 64-site configuration, volume conduction effects after the surface-Laplacian transform are minimal beyond the distance between adjacent sites (e.g., Cohen, 2014). Because the relevant effects were similar across all regions, we re-examined them for a state trajectory of a global array comprising 16 non-adjacent sites (with the minimum inter-site distance being twice the original inter-site distance) evenly sampled from the whole scalp (see the scalp map in Figure 8). If spurious volume conduction effects played a substantial role in the original analyses, the effects should minimize in this re-analysis.

All effects persisted. The temporal variation in trajectory instability was significantly elevated relative to the full phase-scrambled control across all time-scales, but it was largely at the same level as the cross-frequency phase-scrambled control (Figure 8A). The time-averaged trajectory speed was significantly reduced relative to the full phase-scrambled controls across all time-scales and it was also significantly reduced relative to the cross-frequency phase-scrambled controls across most time-scales. To confirm the role of cross-site within-frequency phase alignments, the time-averaged trajectory speed was significantly more reduced relative to the full phase scrambled controls than relative to the cross-frequency phase-scrambled controls across all time-scales (Figure 8B; the overlapping error bars representing ±1 regular standard error are not informative for this within-participants comparison; it is clear from the inset that all participants consistently produced the effect). Finally, the temporal variation in trajectory speed was significantly elevated relative to both the full and cross-frequency phase-scrambled controls, and significantly more elevated relative to the full than cross-frequency phase-scrambled controls across all time-scales (Figure 8C). Thus, this analysis has confirmed the original results that only within-frequency phase relations contributed to elevating the temporal variation in trajectory instability, and that both within- and cross-frequency phase relations contributed to reducing the time-averaged trajectory speed and increasing its temporal variation.

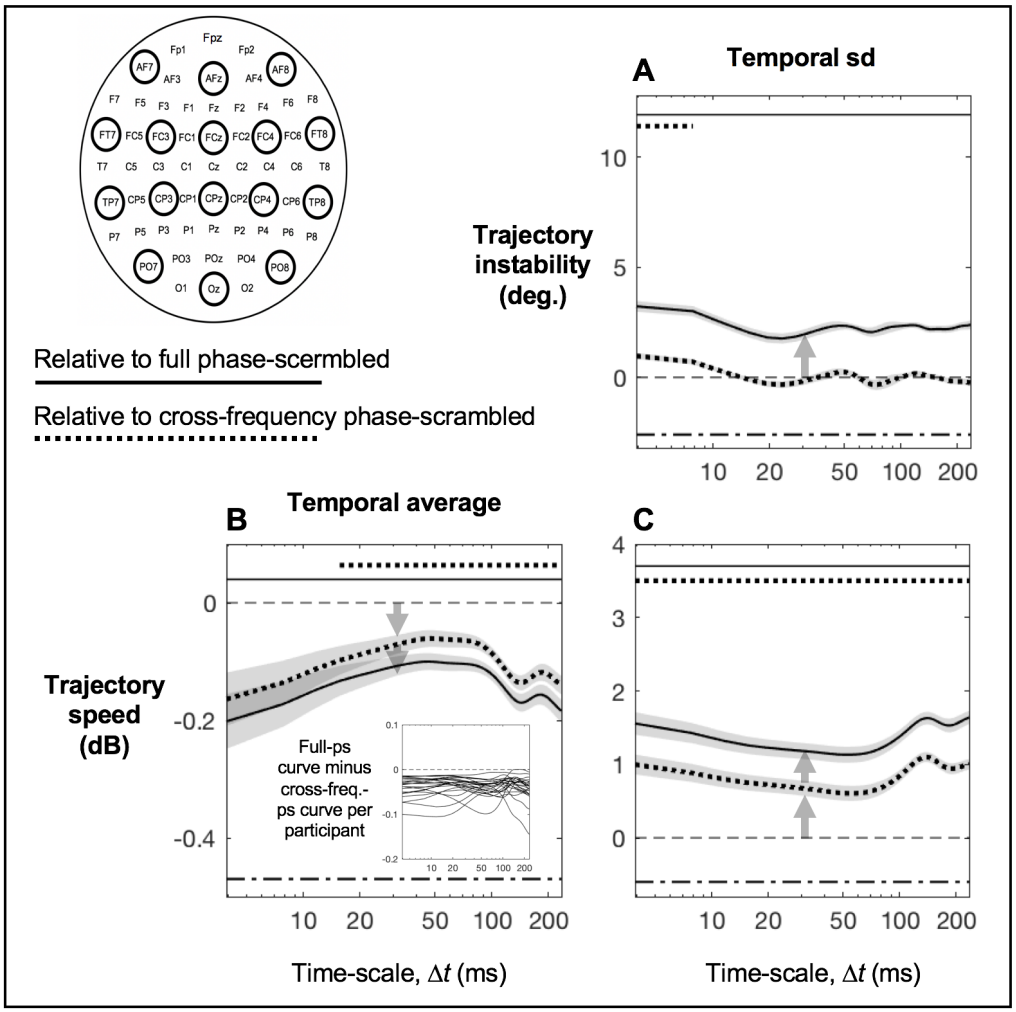

Figure 8. An evaluation of potential contributions of volume conduction to the effects attributable to cross-site phase alignments in EEG (oscillatory or non-oscillatory). Because volume conduction effects are negiligible beyond adjacent scalp sites on a standard 64-site array after the surface-Laplacian transform (Cohen, 2014), we re-computed the effects that may be susceptible to volume conduction (see text) for a global array comprising 16 non-adjacent sites (see upper left). The effects should minimize if volume conduction played substantial roles in the original analyses. The effects relative to the full phase-scrambled cotrols are shown with solid lines and those relative to the cross-frequency phase-scrambled controls are shown with dotted lines. Each horizontal line at the top indicates the time-scale ranges in which the relevant effect significantly differed from the corresponding type of phase-scrambled control; the horizontal line at the bottom indicates the time-scale ranges in which the effect significantly more deviated from the full phase-scrambled control than from the cross-frequency phase-scrambled control (p<0.05 with Bonferroni correction). Unlike in the previous figures, the error bars represent ±1 regular standard error of the mean to emphasize each effect's deviation from the two types of phase-scrambled control. **A.** The temporal variation (measured as standard deviation) in trajectory instability as a function of time-scale Δt relative to the phase-scrambled controls. It is significantly elevated relative to the full phase-scrambled control across all time-scales, but it is not elevated relative to the cross-frequency phase-scrambled control, consistent with the original analyses. **B.** Time-averaged trajectory speed as a function of time-scale Δt relative to the phase-scrambled controls. It is significantly reduced relative to both the full and cross-frequency phase-scrambled controls across most time-scales. The reduction is significantly larger relative to the full phase-scrambled controls than relative to the cross-frequency phase-scrambled controls across all time-scales; while this difference is not evident from the error bars (regular se's), the inset shows that the difference was negative for all participants across all time-scales. These are consistent with the original anlayses. **C.** The temporal variation (measured as standard deviation) in trajectory speed as a function of time-scale Δt relative to the phase-scrambled controls. It is significantly elevated relative to both the full and cross-frequency phase-scrambled controls across all time-scales. The elevation is significantly larger relative to the full phase-scrambled controls than relative to the cross-frequency phase-scrambled controls across all time-scales. These are consistent with the original analyses.

Concluding remarks

A major goal of the current study was to elucidate potential macroscopic principles governing global neural dynamics by examining EEG spatiotemporal state trajectories. This method provides a "birds-eye view" of global neural dynamics that complements the extensive literature built on reductive methods that typically include the computation of instantaneous spectral phase/amplitude at each scalp site followed by analyses of within-frequency and cross-frequency phase relations examined by frequency, by cross-frequency pair, and by site pair. The macroscopic state variables examined in the current study lack the details provided by the pairwise phase-relations analyses, but they offer some complementary advantages. For example, state-trajectory instability and speed may capture emergent properties of global spatiotemporal dynamics that may closely reflect perceptual, attentional, and/or cognitive dynamics. These state variables may also allow relatively quick evaluations of the global coordination of within-frequency and cross-frequency phase relations. Not requiring the computation of instantaneous spectral amplitude/phase circumvents some limitations such as a time-frequency trade-off. Further, while state trajectories directly incorporate EEG spatiotemporal dynamics, the time-scale based analyses of trajectory instability and speed allow comparisons with analyses of spectral-amplitude profiles and phase relations. In addition to providing a complementary non-reductive method to studying EEG spatiotemporal dynamics, the current study has identified some potential general principles governing intrinsic global neural dynamics.

A first potential principle is the tight inter-region convergence of time-averaged state-trajectory instability at the level of ~100° at the time-scale of ~25 ms (Figure 3A-3D). This convergence does not appear to be coincidental as the time-averaged trajectory instability of each region depends on the details of spectral-amplitude profiles across its constituent sites. Further, the fact that both within- and between-participant variability in time-averaged trajectory instability minimized at the time-scale of ~25 ms (Figure 7B-7C) provided indirect evidence suggesting that the convergence may be actively maintained. Thus, the tight convergence may address a fundamental question of why EEG spectral-amplitude profiles at different sites take on their characteristic shapes (e.g., Figure 2), suggesting that a potential organizing principle is to globally maintain (on average) nearly directionally unconstrained but slightly conservative topographic changes at a universal time-scale of ~25 ms. We noted that state trajectories appeared to be overall less constrained (trajectory instability hovering around ~100° over a broad range of time-scales) in the anterior region likely reflecting cognitive processes, whereas they appeared to be more constrained (trajectory instability swinging further away from 90°) in the central and posterior regions, likely reflecting sensory processes. We thus speculated that the observed convergence may suggest that information may be exchanged between the

executive and sensory processes in ~25 ms packets at the matched level of state-trajectory flexibility which may facilitate directionally balanced interactions. A second potential principle is that cross-site within-frequency phase relations contribute to globally (across all regions) increasing the temporal variation in trajectory instability in a relatively time-scale invariant manner. This effect may be accomplished by tightening frequency specific phase alignments of oscillatory activity across sites over a broad range of frequencies. A third potential principle is that both within- and cross-frequency phase relations contribute to globally (across all regions) decreasing time-averaged trajectory speed while increasing its temporal variation in a relatively time-scale invariant manner in dB. These effects may be accomplished by increasing the cross-site synchronization of EEG (not necessarily oscillatory) and by coordinating the temporal structures of within-site EEG waveforms to include sharper and more intermittent changes that are self-similar across time-scales, such that the decreases in time-averaged trajectory speed are divisive and the increases in its temporal variation are multiplicative. A fourth potential principle is that the coordination of phase relations primarily generates positive temporal correlations between state-trajectory instability and speed (relative to the phase-scrambled controls), nudging the spatiotemporal changes of EEG potentials away from being oscillatory (though with some notable differences in the time-scale dependence across the three regions).

A deeper understanding of these potential global principles governing intrinsic neural dynamics will depend on future research investigating how the behaviors of state-trajectory instability and speed adjust while people engage in different behavioral tasks. Some of the global principles of intrinsic dynamics may remain task invariant, indicative of homeostatic processes. Others may characteristically adjust according to cognitive requirements and/or sensory interactions, elucidating their potential functional relevance. Some preliminary results are suggestive of these distinctions. For example, the inter-region convergence of state-trajectory instability at 100° at 25 ms (obtained while participants rested with their eyes closed in the current study) appears to be maintained during viewing of a nature video as well as when people view and rate flickering displays for aesthetic preference. In contrast, the effects of phase relations on state-trajectory instability and speed appear to adjust in a task and stimulus specific manner (Menceloglu, Grabowecky, & Suzuki, unpublished results). In the long run, a fuller understanding of global neural dynamics will emerge from developing computational models that link the mesoscopic mechanisms elucidated by the detailed analyses of pairwise cross-site phase relations to the characteristics of macroscopic variables such as state-trajectory instability and speed examined here. Another avenue would be to use computational simulation to understand how spectral-amplitude profiles, properties of EEG waveforms such as sharpness and intermittency, cross-site within-frequency and cross-frequency phase relations, and the $1/f^{\beta}$ background, influence the time-scale profiles

of state-trajectory instability and speed. Beyond efforts to link global state variables to mesoscopic mechanisms, global analyses of EEG spatiotemporal dynamics as *k*-dimensional trajectories with the use of state variables characterizing various trajectory features such as instability and speed may provide unique macroscopic insights into global neural dynamics, analogous to the concept of temperature providing useful insights into thermodynamic processes. These macroscopic measures of EEG dynamics may also more closely reflect specific types of attentional and cognitive operations, sensory responses, and dysfunctions than more detailed mesoscopic measures.

References

Adebimpe, A., Arabi, A., Bourel-Ponchel, E., Mahmoudzadeh, M., & Wallois, F. (2016). EEG resting state functional connectivity analysis in children with benign epilepsy with centrotemporal spikes. *Frontiers in Neuroscience, 10, Article 143*, 1-9.

Antonakakis, M., Dimitriadis, S. I., Zervakis, M., Micheloyannis, S., Resaie, R., Babajani-Feremi, A., Zouridakis, G., & Papanicolaou, A. C. (2016). Altered cross-frequency coupling in resting-state MEG after mild traumatic brain injury. *International Journal of Psychophysiology, 102*, 1-11.

Cohen, M. X. (2014). *Analyzing Neural Time Series Data: Theory and Practice*, MIT Press.

Dehaene, S., & Changeux, J.-P. (2011). Experimental and theoretical approaches to conscious processing. *Neuron, 70*, 200-227.

Delorme, A., & Makeig, S. (2004). EEGLAB: an open source toolbox for analysis of single-trial EEG dynamics including independent component analysis. *Journal of neuroscience methods*, *134*(1), 9-21.

Donner, T. H., & Siegel, M. (2011). A framework for local cortical oscillation patterns. *Trends in Cognitive Sciences, 15(5)*, 191-199.

Duzel, E., Penny, W. D., & Burgess, N. (2010). Brain oscillations and memory. *Current Opinion in Neurobiology, 20*, 143-149.

Engel, A. K., & Fries, P. (2010). Beta-band oscillations—signaling the status quo? *Current Opinion in Neurobiology, 20*, 156-165.

Fahrenfort, J. J., Scholte, H. S., & Lamme, V. A. (2007). Masking disrupts reentrant processing in human visual cortex. *Journal of cognitive neuroscience*, *19*(9), 1488-1497.

Fries, P. (2005). A mechanism for cognitive dynamics: neural communication through neural coherence. *Trends in Cognitive Sciences, 9(10)*, 474-480.

Gonzalez, G. F., Simt, D. J. A., van der Molen, M. J. W., Tijms, J., Stam, C. J., de Geus, E. J. C., & van der Molen, M. W. (2018). EEG resting state functional connectivity in adult dyslexics using phase lag index and graph analysis. *Frontiers in Human Neuroscience, 12, Article 341*, 1-12.

He, B. J. (2014). Scale-free brain activity: past, present, and future. *Trends in Cognitive Sciences, 18(9)*, 480-487.

Hipp, J. F., Hawellek, D. J., Corbetta, M., Siegel, M., & Engel, A. K. (2012). Large-scale cortical correlation structure of spontaneous oscillatory activity. *Nature Neuroscience, 15(6)*, 884-890.

Hjorth, B (1980). Source derivation simplifies topographical EEG interpretation. *American Journal of EEG Technology 20*, 121-132.

Jann, K., Kottlow, M., Dierks, T., Boesch, C., & Koenig, T. (2010). Topographic electrophysiological signatures of fMRI resting state networks. *PloS ONE*, *5*(9), e12945.

Jensen, O., Gips, B., Bergmann, T. O., & Bonnefond, M. (2014). Temporal coding organized by coupled alpha and gamma oscillations prioritizes visual processing. *Trends in Cognitive Sciences, 37(7)*, 357-369.

Kayser, J., Tenke, C. E. (2006). Principal components analysis of Laplacian waveforms as a generic method for identifying ERP generator patterns: I. Evaluation with auditory oddball tasks. *Clinical Neurophysiology 117*, 348-368.

Klimesch, W. (2012). Alpha-band oscillations, attention, and controlled access to stored information. *Trends in Cognitive Sciences, 16(12)*, 606-617.

Kiya, H., Ito, I., & Miron, S. (2010). "Phase scrambling for image matching in the scrambled domain" in Signal Processing, *InTech*, 97-414.

Koch, C. (1999). *Biophysics of Computation: Information Processing in Single Neurons*. Oxford.

Lamme, V. A., Zipser, K., & Spekreijse, H. (2002). Masking interrupts figure-ground signals in V1. *Journal of cognitive neuroscience*, *14*(7), 1044-1053.

Laufs, H., Krakow, K., Sterzer, P., Eger, E., Beyerle, A., Salek-Haddadi, A., & Kleinschmidt, A. (2003). Electroencephalographic signatures of attentional and cognitive default modes in spontaneous brain activity fluctuations at rest. *Proceedings of the National Academy of Sciences*, *100*(19), 11053-11058.

Lopez-Calderon, J., & Luck, S. J. (2014). ERPLAB: an open-source toolbox for the analysis of event-related potentials. *Frontiers in human neuroscience*, *8*, 213.

Luck, S. J., & Kappenman, E. S. (2012). ERP components and selective attention. *The Oxford handbook of event-related potential components*, 295-327.

Mazzoni, A., Panzeri, S., Logothetis, N. K., & Brunel, N. (2008). Encoding of naturalistic stimuli by local field potential spectra in networks of excitatory and inhibitory neurons. *PLoS Computational Biology, 4(12)*: e1000239. doi:10.1371/journal.pcbi.1000239

Michalareas, G., Vezoli, J., van Pelt, S., Schoffelen, J.-M., Kennedy, H., & Fries, P. (2016). Alpha-beta and gamma rhythms subserve feedback and feedforward influences among human visual cortical areas. *Neuron, 89*, 384-397.

Müller, V., Perdikis, D., Oertzen, T., Sleimen-Malkoun, R, Jirsa, V., & Lindenberger, U. (2016). Structure and topology dynamics of hyper-frequency networks during rest and auditory oddball performance. *Frontiers in Computational Neuroscience, 10, Article 108*, 1-25.

Olejarczyk, E., Marzetti, L., Pizzella, V., & and Zappasodi, F. (2017). Comparison of connectivity analyses for resting state EEG data. *Journal of Neural Engineering, 14, 036017*, 1-13.

Osipoval, D., Hermes, D., & Jensen, O. (2008). Gamma-power is phase-locked to posterior alpha activity. *PLoS ONE, 3(12), e3990*, 1-7.

Palva, S., & Palva, M. (2007). New vistas for a-frequency band oscillations. *Trends in Neurosciences, 30(4)*, 150-158.

Palva, S., & Palva, J. M. (2012). Discovering oscillatory interaction networks with M/EEG: challenges and breakthroughs. *Trends in Cognitive Sciences, 16(4)*, 219-230.

Perrin, F., Pernier, J., Bertrand, O., & Echallier, J. F. (1989a). Corrigenda EEG 02274. *Electroencephalography and Clinical Neurophysiology 76*, 565.

Perrin, F., Pernier, J., Bertrand, O., & Echallier, J. F. (1989b). Spherical Splines for Scalp Potential and Current Density Mapping. *Electroencephalography and Clinical Neurophysiology 72(2)*: 184-187.

Perrin, F., Pernier, J., Bertrand, O., Giard, M. H., & Echallier, J. F. (1987). Mapping of Scalp Potentials by Surface Spline Interpolation. *Electroencephalography and Clinical Neurophysiology, 66 (1)*, 75-81.

Pratt, H. (2011). Sensory ERP components. *The Oxford handbook of event-related potential components*, 89-114.

Scally, B., Burke, M. R., Bunce, D., & Delvenne, J.-F. (2018). Resting-state EEG power and connectivity are associated with alpha peak frequency slowing in healthy aging. *Neurology of Aging, 71*, 149-155.

Smulders, F. T., Miller, J. O., & Luck, S. J. (2012). The lateralized readiness potential. *The Oxford handbook of event-related potential components*, 209-229.

Stankovski, T., Ticcinelli, V., McClintock, P. V. E., & Stefanovska, A. (2017). Neural cross-frequency coupling functions. *Frontiers in Systems Neuroscience, 11, Article 33*, 1-13.

Swaab, T. Y., Ledoux, K., Camblin, C. C., & Boudewyn, M. A. (2012). Language-related ERP components. *The Oxford handbook of event-related potential components*, 397-440.

Tenke, C. E., & Kayser, J. (2012). Generator localization by current source density (CSD): Implications of volume conduction and field closure at intracranial and scalp resolutions. *Clinical Neurophysiology, 123*, 2328–2345.

van Albada, S. J., & Robinson, P. A. (2013). Relationships between electroencephalographic spectral peaks across frequency bands. *Frontiers in Human Neuroscience, 7, A56*, 1-18.

van Beijsterveldt, C. E. M., and van Baal, G. C. M. (2002). Twin and family studies of human electroencephalogram: a review and a meta-analysis. *Biological Psychology, 61*, 111-138.

Varela, F., Lachaux, J.-P., Rodriguez, E., Martinerie, J. (2001). The brain web: phase synchronization and large-scale integration. *Nature Reviews Neuroscience, 2*, 229-239.